Journal of Colloid and Interface Science 683 (2025) 1087–1095

Contents lists available at ScienceDirect

Journal of Colloid And Interface Science

journal homepage: www.elsevier.com/locate/jcis

Regular Article

Electron transfer enhanced flower-like NiP_2-Mo_8P_5 heterostructure synergistically accelerates fast HER kinetics for large-current overall water splitting

Mingcheng Gao [a], Weijie Pan [a], Zhiyang Huang [a], Lixia Wang [a], Jingya Guo [a,*], Sheraz Muhammad [a], Changping Ruan [a,*], Tayirjan Taylor Isimjan [b], Xiulin Yang [a,*]

[a] Guangxi Key Laboratory of Low Carbon Energy Materials, School of Chemistry and Pharmaceutical Sciences, Guangxi Normal University, Guilin 541004, China
[b] Saudi Arabia Basic Industries Corporation (SABIC) at King Abdullah University of Science and Technology (KAUST), Thuwal 23955-6900, Saudi Arabia

HIGHLIGHTS

- A nanoflower-like NiP_2-Mo_8P_5@NF is constructed by a thermal and phosphating strategies.
- The catalyst shows good HER activity (157 mV@100 mA cm^{-2}) and long-term stability.
- The cathode in overall water splitting needs a low cell voltage of 1.67 V at 100 mA cm^{-2}.
- The superior activity results from the synergy of rich heterostructures, high conductivity and good hydrophilicity.

GRAPHICAL ABSTRACT

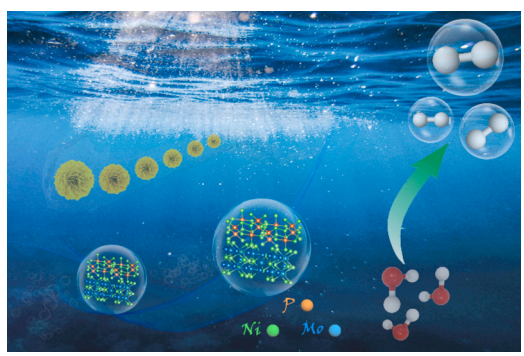

ARTICLE INFO

Keywords:
NiP_2-Mo_8P_5@NF
Heterogeneous structure
Electronic interaction
Hydrogen evolution reaction
Overall water splitting

ABSTRACT

Developing an innovative metal-phosphorus heterostructure as an excellent electrocatalyst for hydrogen evolution reaction (HER) is crucial for achieving large-scale water electrolysis, although it remains challenging. Herein, we introduce a pioneering strategy entailing the coordination of two metal phosphides in a catalytic structure by employing a wide variety of catalytically active species and regulating the electronic structure. Our method involves an extraordinary heterostructure construction with nickel phosphide and molybdenum phosphide formed on nickel foam (NiP_2-Mo_8P_5@NF) through a controlled-solvent thermal and low-temperature phosphorization strategy. Experiments disclose that heterostructure of nickel and molybdenum can effectively modulate the electronic structure of the metal center, foster a robust electronic interaction between Ni and Mo, and induce the formation of rich active sites. The resulting benefits include improved electrical conductivity, which is conducive to synergistically enhancing the electrocatalytic efficiency. Moreover, the NiP_2-Mo_8P_5@NF achieves superhydrophilicity, ensuring effective electrolyte contact and accelerating reaction kinetics. Consequently, NiP_2-Mo_8P_5@NF exhibits favorable HER performance and long-term stability, outperforming commercial Pt/C and most other contemporary electrocatalysts. In practical application, the overall water splitting

* Corresponding authors.
E-mail addresses: jyguo@gxnu.edu.cn (J. Guo), cpruan@mailbox.gxnu.edu.cn (C. Ruan), xlyang@gxnu.edu.cn (X. Yang).

https://doi.org/10.1016/j.jcis.2024.12.143
Received 5 September 2024; Received in revised form 16 December 2024; Accepted 18 December 2024
Available online 19 December 2024

device with NiP_2-Mo_8P_5@NF as cathode delivers a low cell voltage and demonstrates noteworthy durability. This will pave the way for its prospective adoption in industrial water electrolysis applications.

1. Introduction

Water electrolysis, which is powered by renewable energy sources such as solar, wind, or hydropower, has been the subject of growing investigation because of its potential to enable clean and sustainable H_2 generation [1,2]. Nevertheless, a significant obstacle to its commercialization lies in the restricted durability and less-than-ideal performance in hydrogen evolution reactions (HER). These issues substantially diminish energy conversion efficiency and H_2 production rates [3–5]. Currently, the state-of-the-art commercially available catalysts for HER are predominantly noble metal-based materials (for example, Pt, Ir and Ru). Although they possess excellent electrochemical activity, their high cost and limited availability in the Earth's crust severely impede their large-scale utilization in water splitting [6–9]. In light of this, the rational design of electrocatalysts with outstanding performance, structural stability, and cost-effectiveness is of the utmost significance for the practical implementation of water splitting [10].

At present, a wide variety of transition-metal materials have been the subject of extensive research as outstanding catalyst candidates. In particular, transition metal phosphides (TMPs, such as FeP, CoP, NiP_2, and MoP) have yielded promising outcomes due to their hydrogenase-like catalytic mechanism and high activity [11–13]. Among these, nickel phosphide has attracted attention because of its relative abundance and diverse compositions, including Ni_3P, Ni_2P, Ni_5P_4, $Ni_{12}P_5$, NiP_2 and NiP_3 [14–18]. These different phases possess distinct crystal structures that impact the coordination environments of Ni and P, thereby leading to differences in electronic conductivity, corrosion behavior, oxidation rate, and HER activity as a result of varying hydrogen bonding energies [19,20]. As the P:Ni ratio rises in metal phosphides, the number of direct Ni—Ni interactions gradually decreases while the Ni—P coordination increases. For example, pyrite-type NiP_2 has no direct Ni-Ni interactions remaining and exhibits phosphorus-phosphorus bonding (P—P dimer) [21,22]. The electronegativity of P atoms enables them to draw electrons from metal atoms, causing them to function as a base for capturing positively charged protons during HER electrochemical processes [23]. These discoveries imply that the metal-to-phosphorus ratio in the same metal phosphides may play a crucial role in determining HER performance, with more phosphorus-rich phases tending to display higher HER activity [24,25]. However, after numerous investigations on single-phase catalysts, there is only a limited scope for further improvement. Recently, nanocomposites have demonstrated great potential for attaining better HER performance [26,27]. The coordination of two metal phosphides in a catalytic structure has garnered considerable interest due to its ability to provide a diverse range of catalytically active species and regulate the electronic structure of each component via interaction. This permits the adjustment of their capabilities in the adsorption/desorption of reaction intermediates. Research has demonstrated that bimetallic phosphide materials with rich phase edges possess remarkable catalytic activity and robust stability for water-splitting [28,29]. Additionally, molybdenum phosphide has emerged as a capable water splitting electrocatalyst, being earth-abundant, low-cost, and having satisfactory HER performance [30]. Nevertheless, the synthesis of molybdenum phosphide remains a significant obstacle, and novel preparation methods need to be devised. Moreover, the utilization of polymer binders usually augments series resistance and may potentially occlude active sites, impeding diffusion and diminishing effective catalytic activity [31,32]. To surmount these drawbacks and achieve excellent performance, it is preferable to construct a self-supported electrocatalyst with outstanding performance and durability for industrial applications.

Herein, we present a novel self-supported heterogeneous structured catalyst (NiP_2-Mo_8P_5@NF) modified with NiP_2 and Mo_8P_5, which can effectively catalyze both HER and OWS. By varying the solvothermal time and phosphorylation temperature, we are able to modulate the morphological composition of the material, thereby fully exposing the available active sites and significantly improving the conductivity and hydrophilicity to further enhance the catalytic activity. Specifically, the obtained NiP_2-Mo_8P_5@NF demonstrated impressive current densities of 10 mA cm^{-2} and 100 mA cm^{-2} for HER at ultra-low overpotentials of 23 and 157 mV (vs. RHE, Fig. S1), respectively. Furthermore, when assembled into a two-electrode electrolytic cell, the NiP_2-Mo_8P_5@NF catalyst achieved current densities of 10/100 mA cm^{-2} at a low cell voltage of 1.50/1.67 V. Remarkably, the catalyst maintained a stable current density of 100 mA cm^{-2} for 120 h without degradation, indicating its potential for large-scale industrial applications in hydrogen evolution.

2. Experimental section

2.1. Synthesis of NiO-MoO_2@NF nanoflower

All experiments were conducted using deionized (DI) water, and all reagents were of analytical grade and were directly used without further purification. A piece of nickel form (NF) (1.5 cm × 3 cm) was washed with 0.5 M H_2SO_4, ethanol, and deionized water under ultrasonic vibration for 15 min each to eliminate surface impurities. Subsequently, a solution of 1.5 mmol of anhydrous $Na_2MoO_4{\cdot}2H_2O$ and 8 mmol of NH_4F was then dissolved in 25 mL deionized water and stirred at 25 °C. After 10 min, 0.5 mmol of $CO(NH_2)_2$ was added. A solution of 1.5 mmol Ni $(NO_3)_2{\cdot}6H_2O$ was then dissolved in 25 mL deionized water and stirred at 25 °C for 10 min. Finally, the above solution was transferred into a 100 mL Teflon reactor and the previously cleaned NF was immersed and kept at 200 °C for 12, 16, 20 and 24 h (labeled as NiO-MoO_2@NF-12, NiO-MoO_2@NF-16, NiO-MoO_2@NF and NiO-MoO_2@NF-24) in an electric oven, then cooled naturally to room temperature. Finally, the NiO-MoO_2 modified NF was taken out, washed with DI water and ethanol, and then vacuum-dried at 60 °C for 12 h.

2.2. Synthesis of NiP_2-Mo_8P_5@NF nanoflower

The NiP_2-Mo_8P_5@NF nanoflowers (denoted as NiP_2-Mo_8P_5@NF) were synthesized by the low-temperature phosphating method. Specifically, 1.0 g of hypophosphite was weighed and placed upstream of the tube furnace, and a piece of NiO-MoO_2 was positioned downstream of the tube furnace, and then heated at a temperature rate of 400 °C with a ramp rate of 5 °C min^{-1} under N_2 atmosphere for 2 h. For comparison, the NiO-MoO_2@NF-12, NiO-MoO_2@NF-16 and NiO-MoO_2@NF-24 were annealed at the same phosphating temperatures (labeled as NiP_2-Mo_8P_5@NF-12, NiP_2-Mo_8P_5@NF-16, and NiP_2-Mo_8P_5@NF-24), while keeping other conditions constant. Additionally, the NiP_2-Mo_8P_5@NF was annealed for the same phosphating time at different temperatures (denoted as NiP_2-Mo_8P_5@NF-350, NiP_2-Mo_8P_5@NF-450). The mass loading of NiP_2-Mo_8P_5@NF on NF is approximately 2.2 mg cm^{-2}. The catalyst loading was estimated by calculating the weight change of the self-supported catalyst before and after the reaction in a pairwise manner.

2.3. Synthesis of NiP_2-$Ni_2P_4O_{12}$@NF and Mo_8P_5-MoO_2@NF nanosheets

As a comparison, NiP_2-$Ni_2P_4O_{12}$@NF was synthesized using a method akin to the NiP_2-Mo_8P_5@NF synthesis, without using molybdenum as the phosphating precursor. The Mo_8P_5-MoO_2@NF was

produced using Mo_8P_5-MoO_2@NF, the same method was used without the nickel element as the phosphating precursor. Furthermore, the loading of NiP_2-$Ni_2P_4O_{12}$@NF and Mo_8P_5-MoO_2@NF is approximately 2.3 and 1.4 mg cm^{-2}, respectively.

2.4. Synthesis of RuO_2 and Pt/C electrodes

2.2 mg of commercial Pt/C powder or RuO_2 was dispersed in the mixed solution containing 200 μL DI water, 200 μL ethanol, and 10 μL 5 wt.% Nafion. After ultrasonication for 30 min, 200 μL of the above mixture was drop-coated onto the NF surface (1 cm × 1 cm) and dried in air at ambient temperature.

3. Result and discussion

3.1. Synthesis and structural analysis

The NiP_2-Mo_8P_5@NF catalyst was loaded onto a nickel foam substrate through solvent-heated and low-temperature phosphatization process, as illustrated in Scheme 1. The pre-prepared nickel foam substrate was immersed into a Teflon reactor containing a mixed solution of $Ni(NO_3)_2{\cdot}6H_2O$ and $Na_2MoO_4{\cdot}2H_2O$, and then subjected to an oven hydrothermal reaction at 200 °C for 20 h. Once the reaction was completed, the substrate was removed from the reactor. However, the nickel diffraction peaks of NiP_2-Mo_8P_5 on the NF were prominent, potentially masking the diffraction peaks of other substances. To address this issue, the powder at the bottom of the reaction kettle was collected through centrifugation. This powder was then synthesized using the same low-temperature phosphatization method for further XRD studies.

As depicted in Fig. 1a, the diffraction peaks of NiP_2-Mo_8P_5 were indexed to NiP_2 (JCPDS: 75–1519) [33] and Mo_8P_5 (JCPDS: 77–2006), respectively. One notable feature is the complete transformation of NiO-MoO_2@NF into a new structure NiP_2-Mo_8P_5@NF after low-temperature phosphating. This new two-phase heterostructure, obtained at 400 °C, may be one of the main reasons for the improved electrochemical properties. Additionally, the XRD pattern of NiO after low-temperature phosphorylating showed the presence of a new NiP_2 phase (Fig. S2), which further highlighting the impact of low-temperature phosphating. The surface area and pore size of NiP_2-Mo_8P_5@NF were determined using N_2 adsorption–desorption isotherm. To perform the Brunauer-Emmett-Taylor (BET) surface area analysis, approximately 100 mg of NiP_2-Mo_8P_5 was stripped from the nickel foam substrate. As shown in Fig. 1b, NiP_2-Mo_8P_5@NF exhibits a specific surface area of 22.105 m^2 g^{-1} and an average pore size of 16.1885 nm. This large BET surface area, combined with its unique mesoporous structure, enhances electrolyte transport and accelerates the mobility of catalytic reactants to HER active sites, thereby reducing mass transfer resistance [34]. Scanning electron microscopy (SEM) was used to examine the morphology and microstructure of the different materials. Fig. 1c illustrates the nanoflower-like morphology of NiP_2-Mo_8P_5@NF with a smooth surface. In contrast, NiP_2-$Ni_2P_4O_{12}$@NF and Mo_8P_5-MoO_2@NF exhibit less regular nanosheet and coral-mounted morphologies, respectively (Fig. S3). Scanning electron microscopy (SEM) images of NiP_2-Mo_8P_5@NF at different hydrothermal times reveal a transformation from an irregular structure to a well-defined nanoflower morphology. After 24 h of hydrothermal treatment, the nanoflower morphology gradually transforms into nanorod, eventually covering the active sites. These findings indicate that hydrothermal treatments duration is crucial for the material's morphology development (Fig. S4). Additionally, the effect of phosphating temperature on the material's morphology was investigated. SEM images confirmed the formation of irregular and nanorod-shaped morphologies at various phosphating temperatures (Fig. S5). These results suggest that phosphating temperatures significantly influences the material's morphology and imply that the nanoflower structure is conducive to mass transfer and gas diffusion. The nanoflower morphology of NiP_2-Mo_8P_5@NF was further analyzed using transmission electron microscopy (TEM). As shown in Fig. 1d inset, the TEM images corroborate the SEM observations. High-resolution TEM (HR-TEM) images revealed lattice fringes with spacings of 0.1828 nm and 0.2259 nm, corresponding to the (200) and (400) planes of NiP_2 and Mo_8P_5, respectively (Fig. 1d), confirming the presence of a two-phase structure. Moreover, the selected area electron diffraction (SAED) pattern (Fig. 1e) shows diffraction rings attributable to the (200) and (400) planes of NiP_2 and Mo_8P_5. These findings align with the XRD and HR-TEM results, further verifying that NiP_2 and Mo_8P_5 exist as distinct single crystals [35]. Energy dispersive X-ray spectroscopy (EDS) confirmed the coexistence of Ni, Mo, and P elements (Fig. S6). Additionally, the actual Ni/Mo contents in the different catalysts were quantified using inductively coupled plasma mass spectrometry (ICP-MS) (Table S1). In addition, high-angle annular dark-field scanning TEM (HAADF-STEM) verified the nanoflower-like structure, and elemental mapping showed that the elements Ni, Mo, P, and C were uniformly distributed throughout the nanoflower (Fig. 1f).

X-ray photoelectron spectroscopy (XPS) was employed to further investigate the elemental composition and chemical valence states of the as-obtained catalysts. The full-range XPS investigation of NiP_2-Mo_8P_5@NF, Mo_8P_5-MoO_2@NF and NiP_2-$Ni_2P_4O_{12}$@NF (Fig. S7a) revealed that these materials clearly show the presence of Ni, P, O, and C elements. NiP_2-Mo_8P_5@NF and Mo_8P_5-MoO_2@NF both exhibit the presence of Mo elements in contrast to NiP_2-$Ni_2P_4O_{12}$@NF, indicating the successful introduction of Mo, these results align well with the elemental mappings and EDS patterns showcased in Fig. 1f and Fig. S6. The high-resolution C 1 *s* spectrum of NiP_2-Mo_8P_5@NF is calibrated as C—C (284.8 eV), C—O (286.0 eV) and –O—C═O (288.0 eV) (Fig. S7b). As deconvoluted in the high-resolution spectra of Ni 2*p* (Fig. 2a), the peaks at 855.3, 857.1 and 861.0 eV can be indexed to Ni^{2+} $2p_{3/2}$, Ni^{3+} $2p_{3/2}$ and Sat. Ni, respectively[36,37], indicating the formation of nickel-oxygen species. In addition, a peak at 852.4 eV was identified as

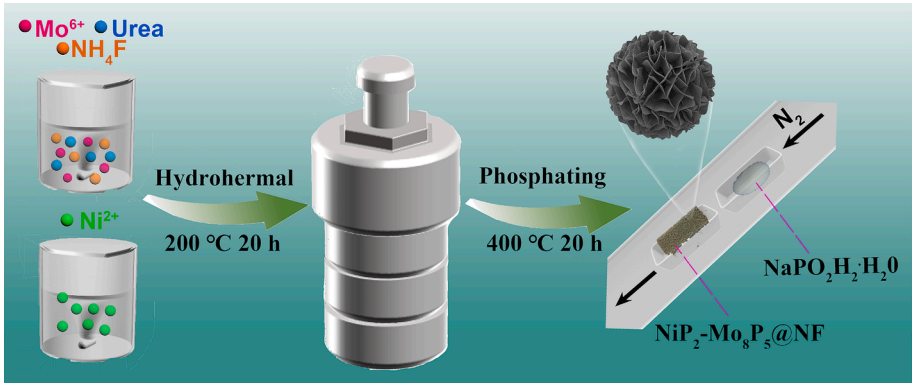

Scheme 1. Schematic illustration of the synthesis of NiP_2-Mo_8P_5@NF.

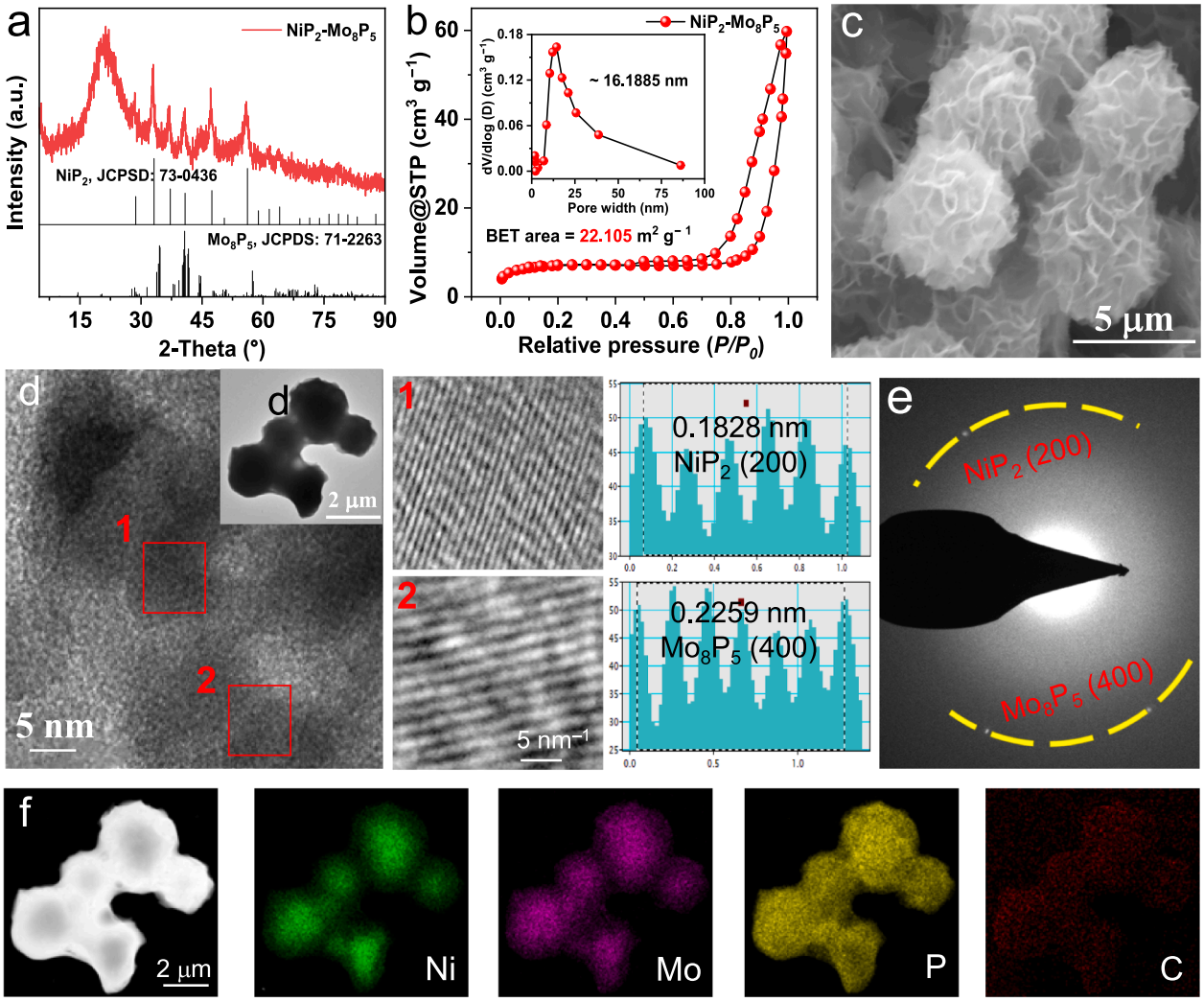

Fig. 1. (a) XRD pattern of NiP_2-Mo_8P_5 . (b) N_2 adsorption–desorption isotherms and pore-size distribution curves of NiP_2-Mo_8P_5@NF. (c) SEM image of NiP_2-Mo_8P_5@NF. (d) HR-TEM image and the corresponding lattice spacing profiles of the dotted line regions (inset: Low-magnification TEM image of NiP_2-Mo_8P_5@NF). (e) Selected area electron diffraction (SAED) pattern, and (f) HAADF-STEM image and EDS elemental mapping of Ni, Mo, P and C of NiP_2-Mo_8P_5@NF.

Ni-P species [38], confirming that the successful formation of NiP_2 and the nickel-phosphide bond in the HER reaction. Peculiarly, the observed decrease in the binding energy of Ni 2*p* in NiP_2-Mo_8P_5@NF, compared to that in NiP_2-$Ni_2P_4O_{12}$@NF suggests that the incorporation of Mo can regulate the electronic state of Ni, resulting in the formation of a low-valence Ni state and facilitating a strong Ni-Mo electronic interaction, which is beneficial for enhancing HER activity. The incorporation of new transition metal cations resulted in smaller peaks corresponding to oxidized species in both the Mo 3*d* region. TMP surfaces are widely known to spontaneously oxidize upon exposure to air, resulting in easily observed transition metal oxides on their surfaces. Furthermore, The Mo 3*d* spectrum of MoP shows peaks corresponding to two double characteristic peaks: Mo^{6+} (231.8/232.7 eV), and $Mo^{\delta+}$ (230.0/230.9 eV) (Fig. 2b) [39–41]. The existence of high-valent Mo species might indicate the formation of oxidized species, while the $Mo^{\delta+}$ ($0 < \delta^{+} < 4$) peaks are generally considered corresponding to Mo-P bonding in the TMPs [42]. In particular, the Mo 3*d* peak of NiP_2-Mo_8P_5@NF is gradually positively shifted to a higher energy level compared to that of Mo_8P_5-MoO_2@NF, the shift in the Mo peaks might indicate that highly oxidized species have accepted extra electron density from the Ni atoms. The NiP_2-Mo_8P_5@NF exhibited an analogous trend in its peak area ratio, showing fewer Mo^{6+} species and more Mo—P bonding after the addition of Ni cations. Enhanced catalytic activity following the post-synthetic transformation can be understood in terms of chemical state changes. Metal oxides are well known to not only block catalytically active sites for HER but also to cause high resistance to charge transfer [43,44]. Because TMPs are easily oxidized when exposed to air, excessive oxidation needs to be prevented to alleviate any deterioration in HER activity, especially for small nanocatalysts with large surface areas. The introduction of a foreign metal cation with lower electronegativity might alleviate TMP catalyst degradation by providing extra electron density and restraining oxidation of the catalyst surface [45]. The abundant Mo-P bonds and higher HER performance of NiP_2-Mo_8P_5@NF might be due to the greater difference in electronegativity between the original metal (Mo) and the additional metal (Ni) compared to that of Mo_8P_5-MoO_2@NF, as revealed by the relationship between HER activity difference. The P 2*p* region of NiP_2-Mo_8P_5@NF is deconvoluted into three peaks at 129.0, 130.0, and 133.9 eV (Fig. 2c), which are attributed to $2p_{3/2}$ and $2p_{1/2}$ of Ni—P or Mo—P and P—O bonds due to surface oxidation caused by phosphorus [46–48]. Moreover, the O 1 *s* XPS spectrum of NiP_2-Mo_8P_5@NF is presented in Fig. S7c. The peaks located at 530.7, and 532.3 eV of the obtained electrocatalysts are ascribed to carbon–oxygen (C—O) and adsorbed water molecules (H_2O_{ads}), respectively [49]. To further confirm the hydrophilic property, the contact angle (CA) test was performed as shown in Fig. 2d. The results show a reduction of 14.5° in the contact angle after the phosphating process, indicating the improved hydrophilicity [50,51]. Therefore, the heterostructure of NiP_2 and Mo_8P_5 not only skillfully regulates the

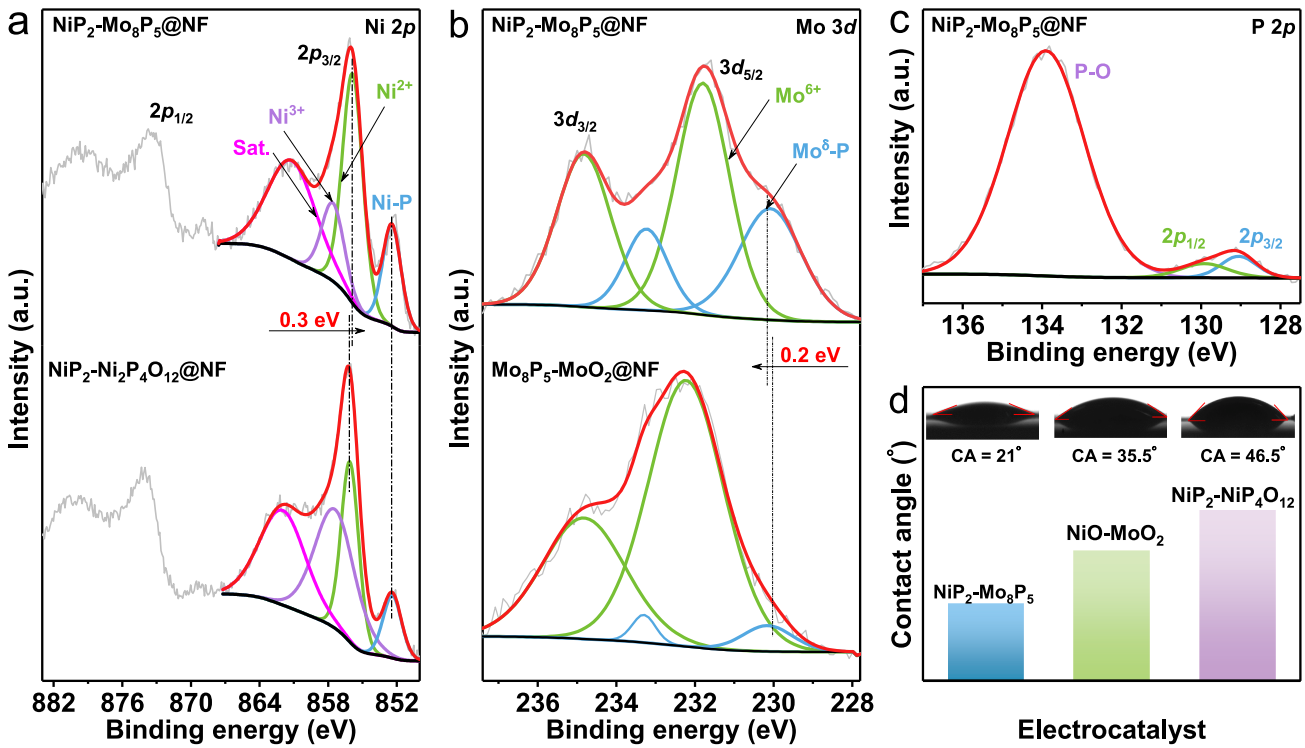

Fig. 2. High-resolution X-ray photoelectron spectra (XPS). (a) Ni 2*p* of NiP_2-Mo_8P_5@NF and NiP_2-$Ni_2P_4O_{12}$ @NF. (b) Mo 3*d* of NiP_2-Mo_8P_5@NF and Mo_8P_5-MoO_2@NF. (c) P 2*p* of NiP_2-Mo_8P_5@NF. (d) Contact angle images of NiP_2-Mo_8P_5 , NiO-MoO_2 and NiP_2-$Ni_2P_4O_{12}$, respectively.

electronic structure of Ni and Mo, but also enhances their hydrophilicity, thereby improving the catalytic performance.

3.2. Electrochemical performance for HER

The hydrogen evolution reaction (HER) efficiency of the devised catalysts was evaluated using a standard three-electrode setup in a 1.0 M KOH medium. The optimal NiP_2-Mo_8P_5@NF catalyst was obtained when the solvent heating time was 20 h and the phosphating temperatures was 400 °C (Fig. S9-S12). Thenceforth, for simplicity, the catalyst will be referred to as NiP_2-Mo_8P_5@NF.

As shown in Fig. 3a, the linear scanning voltammetry (LSV) curves compare the performances of NiP_2-Mo_8P_5@NF, NiP_2-$Ni_2P_4O_{12}$@NF, Mo_8P_5-MoO_2@NF, NiO-MoO_2@NF, and Pt/C@NF catalysts, among these catalysts, NiP_2-Mo_8P_5@NF exhibits the most superior HER activity. The NiP_2-Mo_8P_5@NF catalyst required only a low overpotential of 23 mV to drive a current density of 10 mA cm^{-2}, outperforming the other catalysts. Meanwhile, NiP_2-Mo_8P_5@NF exhibited excellent performance with overpotentials of 23, 115, and 157 mV at current densities of 10, 50, and 100 mA cm^{-2}, respectively (Fig. 3b). Importantly, NiP_2-Mo_8P_5@NF consistently maintained a catalytic activity comparable to that of Pt/C@NF as the current density increased. To gain insight into the reaction kinetics, we derived the corresponding Tafel slopes from the polarization curves (Fig. 3c). The tafel slope of NiP_2-Mo_8P_5@NF (87.1 mV dec^{-1}) was significantly lower than NiP_2-$Ni_2P_4O_{12}$@NF (96.3 mV dec^{-1}), Mo_8P_5-MoO_2@NF (113.7 mV dec^{-1}) and NiO-MoO_2@NF (93.8 mV dec^{-1}), indicating that the formation of NiP_2 and Mo_8P_5 two-phase structures greatly accelerated the HER kinetics. Moreover, the excellent HER performance of NiP_2-Mo_8P_5@NF surpassed most of the recently reported HER catalysts (Fig. 3d and Table S2). As shown in Fig. 3e, NiP_2-Mo_8P_5@NF had the lowest charge transfer resistance (R_{ct}) compared with NiP_2-$Ni_2P_4O_{12}$@NF, Mo_8P_5-MoO_2@NF, NiO-MoO_2@NF, and Pt/C@NF, suggesting that the prepared catalysts possessed the fastest electron transfer rate during HER and the introduction of phosphorus elements favored the improvement of electrical conductivity. Electrochemical measurements were performed to evaluate the electrochemical double layer capacitance (C_{dl}) in the non-Faraday region at different scan rates (Fig. S8). It was observed that the C_{dl} value of NiP_2-Mo_8P_5@NF (104.46 mF cm^{-2}) was significantly higher than that of NiP_2-$Ni_2P_4O_{12}$@NF (61.19 mF cm^{-2}), Mo_8P_5-MoO_2@NF (12.57 mF cm^{-2}), and NiO-MoO_2@NF (6.07 mF cm^{-2}) (Fig. 3f), indicating that the NiP_2-Mo_8P_5@NF was able to expose more active sites for HER. The electrochemically active surface area (ECSA) of the samples was evaluated to understand the source of the significant HER activity (Fig. 3g). The highest ECSA was observed for NiP_2-Mo_8P_5@NF (1741 cm^2), indicating that the introduction of the P element can effectively increase the number of active sites and maximize the contact opportunities between the active ingredient and the reactants, thus accelerating the HER process. In order to assess the durability, a chronopotentiometric test was performed. As shown in Fig. 3h, digital photographs of the standard three-electrode system in 1.0 M KOH showed that NiP_2-Mo_8P_5@NF could stably precipitate hydrogen over a long period of time, and the polarization curves of NiP_2-Mo_8P_5@NF after 1000 consecutive CV cycles closely overlapped with the original curves, demonstrating its performance stability. In addition, NiP_2-Mo_8P_5@NF was able to operate continuously for 180 h at a current density of 10 mA cm^{-2} with minimal changes, further demonstrating its strong durability. In comparison, long-term stability tests of NiP_2-$Ni_2P_4O_{12}$@NF (10 h), Mo_8P_5-MoO_2@NF (30 h), and NiO-MoO_2@NF (20 h) revealed significantly poorer durability than NiP_2-Mo_8P_5@NF (Fig. S13). Post-stability testing, the morphology and surface chemical composition of NiP_2-Mo_8P_5@NF were analyzed using SEM and XPS (Fig. S14 and Fig. S15). The SEM results revealed that the surface of the nanoflower became rougher after the long-term stability test, likely due to the natural adsorption of hydroxide from the electrolyte at defect sites. However, the overall morphology remained unchanged, demonstrating the catalyst's excellent structural stability during HER. Interestingly, slight changes in the chemical composition of the catalyst surface were observed. As depicted in Fig. S15, the emergence of metal–oxygen (M−O) bonds was attributed to the natural oxidation of hydroxide

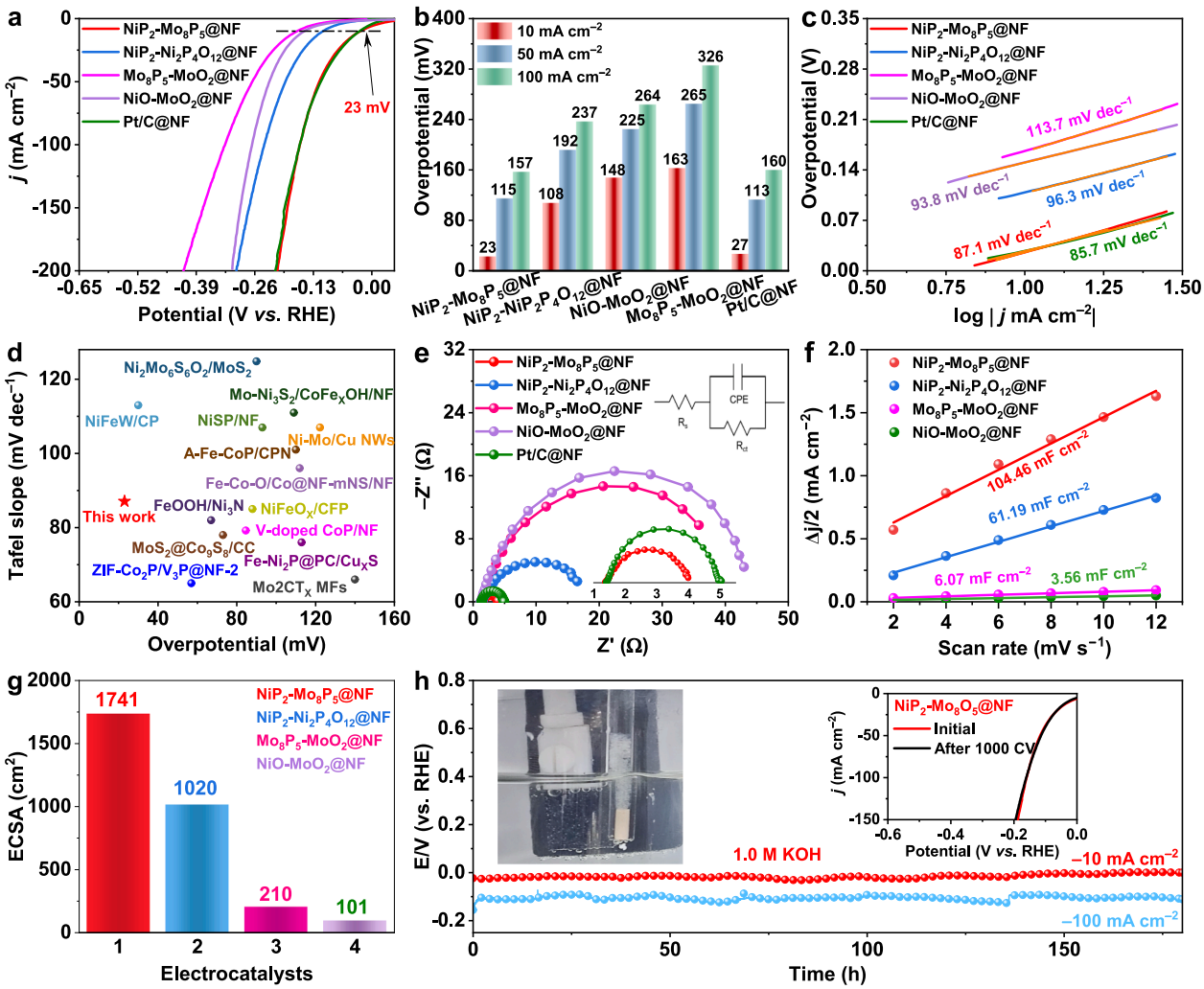

Fig. 3. HER performance of different catalysts in 1.0 M KOH. (a) LSV polarization curves at a scan rate of 2 mV/s . (b) Comparison of the overpotential at 10, 50, and 100 mA cm^{-2} . (c) Tafel plots of different catalysts. (d) Comparison of the overpotential at 10 mA cm^{-2} and the Tafel slope with previously reported HER catalysts. (e) Electrochemical impedance spectroscopy (EIS) data of prepared catalysts. (f) Double-layer capacitance (C_{dl}) plots. (g) Comparison of ECSA for four catalysts. (h) Chronopotentiometry test of NiP_2-Mo_8P_5@NF at 10 mA and 100 cm^{-2} , respectively, (inset: a digital photograph of the standard three-electrode system in 1.0 M KOH, polarization curves of NiP_2-Mo_8P_5@NF before and after 1000 cycles).

species from the electrolyte attaching to these defect sites during the HER process. These findings underscore the strong durability and structural of NiP_2-Mo_8P_5@NF in HER applications.

3.3. Electrochemical performance for OWS

Motivated by the exceptional HER performance and durability of NiP_2-Mo_8P_5@NF, a two-electrode system was assembled with NiP_2-Mo_8P_5@NF and RuO_2@NF as the cathode and anode (denoted as NiP_2-Mo_8P_5@$NF^{(-)}$ || RuO_2@$NF^{(+)}$) to drive overall water splitting (Fig. 4a). As presented in Fig. 4b, the NiP_2-Mo_8P_5@$NF^{(-)}$ || RuO_2@$NF^{(+)}$ system exhibits magnificent overall water splitting performance in 1.0 M KOH, which requires delivering an ultra-low cell voltage of 1.50 at the current density of 10 mA cm^{-2}, which outperforms the commercial Pt/C@$NF^{(-)}$ || RuO_2@$NF^{(+)}$ system. Impressively, with increasing current density, the superiority of NiP_2-Mo_8P_5@NF becomes evident, outstripping the Pt/C@$NF^{(-)}$ || RuO_2@$NF^{(+)}$. The two-electrode water splitting device highlights the limitations of commercial powder-based Pt/C and RuO_2 electrodes, including detachment and reduced activity at high currents due to polymer binders. In contrast, the self-supported binder-free electrodes exhibit superior conductivity, structural robustness, and enhanced catalytic activity, significantly improving overall water-splitting performance. Additionally, the overall water-splitting efficiency of NiP_2-Mo_8P_5@$NF^{(-)}$ || RuO_2@$NF^{(+)}$ surpasses that of most previously reported electrocatalysts at both 10 mA cm^{-2} and 100 mA cm^{-2}, as shown in Fig. 4c and detailed in Table S3. Moreover, a critical parameter for industrial viability is the stability of the system. The electrochemical durability of NiP_2-Mo_8P_5@$NF^{(-)}$ || RuO_2@$NF^{(+)}$ was investigated using chronoamperometry testing. As illustrated in Fig. 4d, NiP_2-Mo_8P_5@$NF^{(-)}$ || RuO_2@$NF^{(+)}$ can maintain stable operation for over 120 h at a current density of 100 mA cm^{-2}. These results demonstrate its noteworthy durability and highlight its potential as a promising non-noble metal alternative for industrial applications.

In addition, the outstanding performance of NiP_2-Mo_8P_5@NF in HER can be attributed to a series of strategic improvements and material properties. These key factors can be attributed to the following aspects: (I) Advanced nanoflower structure: Nanoflower structure can significantly increase the specific surface area and promote efficient electrolyte transport and gas emission [52,53]. (II) Heterostructure construction and electronic modulation: Low-temperature phosphorylation can effectively form heterostructures and generate abundant active sites, which in turn modulate the electronic structure of the metal Ni and Mo centers, improve electrical conductivity, and optimize the adsorption of reaction intermediates, thus enhancing the

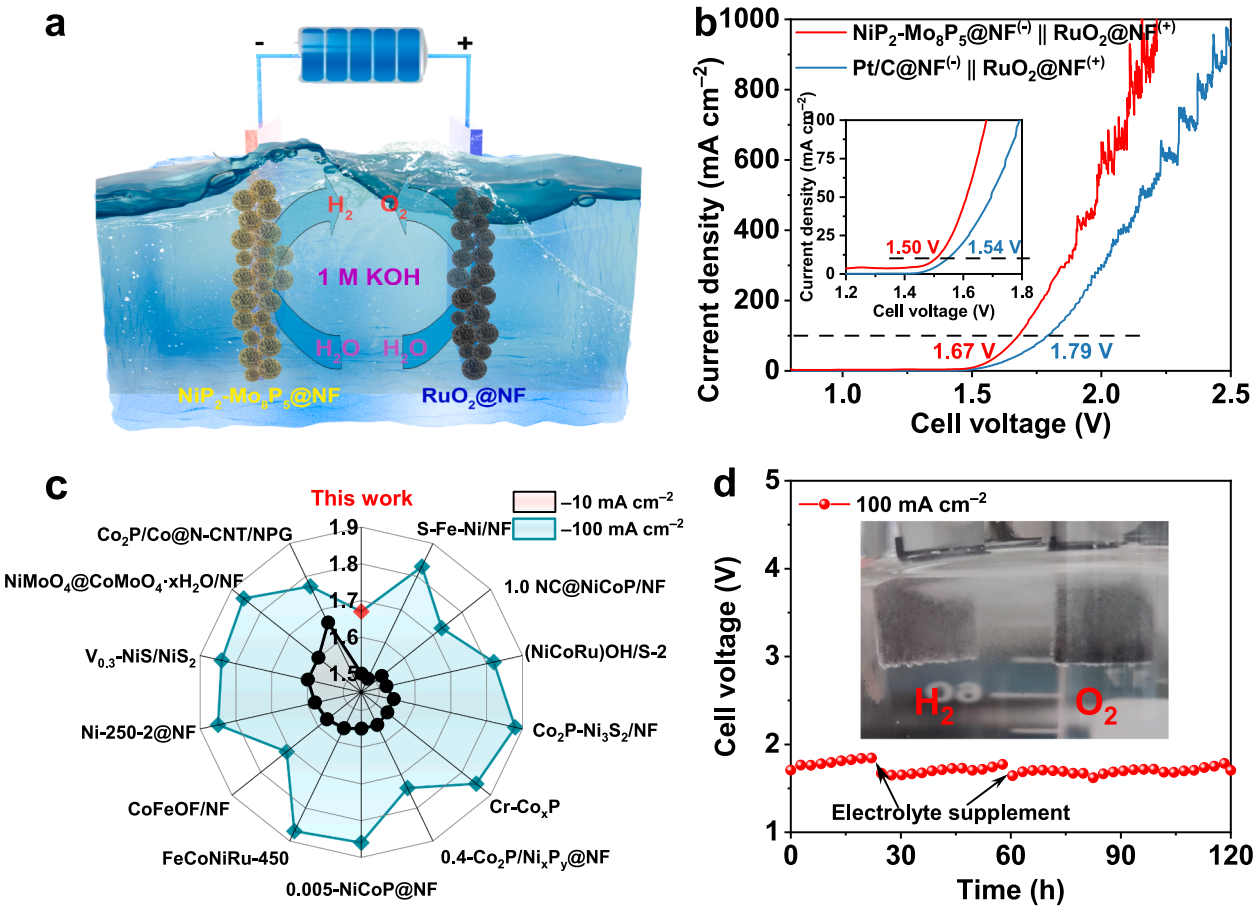

Fig. 4. (a) Schematic diagram of the two-electrode overall water splitting system. (b) LSV curves of the OWS for NiP_2-Mo_8P_5@NF$^{(-)}$ || RuO_2@NF$^{(+)}$ and Pt/C@NF$^{(-)}$ || RuO_2@NF$^{(+)}$ (inset: the cell voltages at low current densities). (c) Comparison of the cell voltages at current densities of 10 mA cm^{-2} and 100 mA cm^{-2} with recently reported catalysts. (d) Chronopotentiometric curve at a current density of 100 mA cm^{-2} for NiP_2-Mo_8P_5 @NF$^{(-)}$ || RuO_2@NF$^{(+)}$ (inset: a digital photograph of the two-electrode OWS system).

conformational activity of the catalyst [54]. (III) Self-supported electrode design: The as-prepared self-supported binder-free electrodes possess excellent conductivity, robust skeleton and large surface area, and thus effectively increasing the contact area, reducing the series resistance, exposing the active sites, promoting diffusion, and further accelerating electron transfer in the electrocatalytic process [55]. (IV) Enhanced hydrophilicity: The heterogeneous structure can effectively regulate the hydrophilicity of the electrocatalytic material, provide stronger capillary force, and promote the contact between the active sites and the reactants, thus paving the way for faster reaction kinetics [51,56]. (V) Specific surface area: The large surface area and its unique mesoporous structure, which promotes the electrolyte transport and accelerates the mobility of catalytic reactants to HER active sites, thereby reducing mass transfer resistance [34].

4. Conclusion

In summary, we present the significant contribution of the phosphorus-rich material NiP_2 and the incorporation of the innovative molybdenum-phosphorus compound Mo_8P_5 to HER and OWS activity. The introduction of Ni and Mo elements substantially enhances the surface properties, rendering it superhydrophilic and thereby attaining excellent electrolyte wettability. Additionally, Mo effectively modulates the electronic structure of the Ni active center, giving rise to a robust electronic interaction between Ni and Mo. This interaction is advantageous for facilitating rapid charge transfer and augmenting electrical conductivity. Consequently, the fabricated NiP_2-Mo_8P_5@NF attains a remarkably low overpotential of 23 mV at 10 cm^{-2} and a diminutive Tafel slope of 87.1 mV dec^{-1}. Its performance eclipses that of commercial Pt/C and exhibits long-term stability exceeding 180 h. Simultaneously, the NiP_2-Mo_8P_5@NF$^{(-)}$ || RuO_2@NF$^{(+)}$ configuration showcases an ultra-low cell voltage of 1.50 V/1.67 V at 10/100 mA cm^{-2}, outstripping the performance of Pt/C@NF$^{(-)}$ || RuO_2@NF$^{(+)}$, thus intimating its potential for industrial implementation. This research offers an illuminating framework for the future design of highly active HER electrocatalysts as alternatives to noble metals.

CRediT authorship contribution statement

Mingcheng Gao: Writing – original draft, Investigation, Data curation. **Weijie Pan:** Data curation. **Zhiyang Huang:** Methodology, Investigation. **Lixia Wang:** Methodology, Data curation. **Jingya Guo:** Writing – review & editing. **Sheraz Muhammad:** Writing – review & editing. **Changping Ruan:** Supervision. **Tayirjan Taylor Isimjan:** Writing – review & editing. **Xiulin Yang:** Writing – review & editing, Supervision.

Declaration of competing interest

The authors declare that they have no known competing financial interests or personal relationships that could have appeared to influence the work reported in this paper.

Acknowledgements

This work has been supported by the National Natural Science

Foundation of China (no. 21965005, 52363028), Natural Science Foundation of Guangxi Province (2021GXNSFAA076001), and Guangxi Technology Base and Talent Subject (GUIKE AD18126001, GUIKE AD20297039).

Appendix A. Supplementary data

Supplementary data to this article can be found online at https://doi.org/10.1016/j.jcis.2024.12.143.

Data availability

The data that has been used is confidential.

References

[1] Y. Lei, Y. Wang, Y. Liu, C. Song, Q. Li, D. Wang, Y. Li, Designing Atomic Active Centers for Hydrogen Evolution Electrocatalysts, Angew. Chem. Int. Ed. 59 (2020) 20794–20812, https://doi.org/10.1002/anie.201914647.

[2] D. Liu, X. Li, S. Chen, H. Yan, C. Wang, C. Wu, Y.A. Haleem, S. Duan, J. Lu, B. Ge, P. M. Ajayan, Y. Luo, J. Jiang, L. Song, Atomically dispersed platinum supported on curved carbon supports for efficient electrocatalytic hydrogen evolution, Nat. Energy 4 (2019) 512–518, https://doi.org/10.1038/s41560-019-0402-6.

[3] J. Chen, Q. Long, K. Xiao, T. Ouyang, N. Li, S. Ye, Z.-Q. Liu, Vertically-interlaced NiFeP/MXene electrocatalyst with tunable electronic structure for high-efficiency oxygen evolution reaction, Sci. Bull. 66 (2021) 1063–1072, https://doi.org/10.1016/j.scib.2021.02.033.

[4] L. Yang, Z. Liu, S. Zhu, L. Feng, W. Xing, Ni-based layered double hydroxide catalysts for oxygen evolution reaction, Mater. Today Phys. 16 (2021) 100292, https://doi.org/10.1016/j.mtphys.2020.100292.

[5] Y. Liu, Q. Feng, W. Liu, Q. Li, Y. Wang, B. Liu, L. Zheng, W. Wang, L. Huang, L. Chen, X. Xiong, Y. Lei, Boosting interfacial charge transfer for alkaline hydrogen evolution via rational interior Se modification, Nano Energy 81 (2021) 105641, https://doi.org/10.1016/j.nanoen.2020.105641.

[6] H. Sun, X. Xu, Y. Song, W. Zhou, Z. Shao, Designing High-Valence Metal Sites for Electrochemical Water Splitting, Adv. Funct. Mater. 31 (2021) 2009779, https://doi.org/10.1002/adfm.202009779.

[7] M. Yang, C.H. Zhang, N.W. Li, D. Luan, L. Yu, X.W. Lou, Design and Synthesis of Hollow Nanostructures for Electrochemical Water Splitting, Adv. Sci. 9 (2022) 2105135, https://doi.org/10.1002/advs.202105135.

[8] X. Li, X. Lv, X. Sun, C. Yang, Y.-Z. Zheng, L. Yang, S. Li, X. Tao, Edge-oriented, high-percentage 1T′-phase MoS_2 nanosheets stabilize Ti_3C_2 MXene for efficient electrocatalytic hydrogen evolution, Appl. Catal. B Environ. Energy 284 (2021) 119708, https://doi.org/10.1016/j.apcatb.2020.119708.

[9] Y.Z. Wang, M. Yang, Y.-M. Ding, N.-W. Li, L. Yu, Recent Advances in Complex Hollow Electrocatalysts for Water Splitting, Adv. Funct. Mater. 32 (2022) 2108681, https://doi.org/10.1002/adfm.202108681.

[10] X.-K. Wan, H.B. Wu, B.Y. Guan, D. Luan, X.W. Lou, Confining Sub-Nanometer Pt Clusters in Hollow Mesoporous Carbon Spheres for Boosting Hydrogen Evolution Activity, Adv. Mater. 32 (2020) 1901349, https://doi.org/10.1002/adma.201901349.

[11] P.W. Menezes, A. Indra, C. Das, C. Walter, C. Göbel, V. Gutkin, D. Schmeiβer, M. Driess, Uncovering the Nature of Active Species of Nickel Phosphide Catalysts in High-Performance Electrochemical Overall Water Splitting, ACS Catal. 7 (2017) 103–109, https://doi.org/10.1021/acscatal.6b02666.

[12] P. Xiao, W. Chen, X. Wang, A Review of Phosphide-Based Materials for Electrocatalytic Hydrogen Evolution, Adv. Energy Mater. 5 (2015) 1500985, https://doi.org/10.1002/aenm.201500985.

[13] Y. Tan, H. Wang, P. Liu, Y. Shen, C. Cheng, A. Hirata, T. Fujita, Z. Tang, M. Chen, Versatile nanoporous bimetallic phosphides towards electrochemical water splitting, Energy Environ. Sci. 9 (2016) 2257–2261, https://doi.org/10.1039/C6EE01109H.

[14] W. Xu, Y. Chen, M. Niederberger, E. Tervoort, J. Mei, D.-L. Peng, Self-Assembled Preparation of Porous Nickel Phosphide Superparticles with Tunable Phase and Porosity for Efficient Hydrogen Evolution, Small 20 (2024) 2309435, https://doi.org/10.1002/smll.202309435.

[15] P. Gao, Y. Zhang, M. Wang, W. Yu, Z. Yan, J. Li, Cost-efficient sunlight-driven thermoelectric electrolysis over Mo-doped Ni_5P_4 nanosheets for highly efficient alkaline water/seawater splitting, J. Mater. Sci. Technol. 211 (2025) 134–144, https://doi.org/10.1016/j.jmst.2024.05.019.

[16] D. Malhotra, T.H. Nguyen, D.T. Tran, V.A. Dinh, N.H. Kim, J.H. Lee, Triphasic Ni_2P–$Ni_{12}P_5$–Ru with Amorphous Interface Engineering Promoted by Co Nano-Surface for Efficient Water Splitting, Small 2309122 (2025), https://doi.org/10.1002/smll.202309122.

[17] B. An, R. Bian, J. Dong, W. Liu, H. Su, N. Li, Y. Gao, L. Ge, Theoretical and experimental investigation on electrostatic field dynamics of Co_3O_4@NiP_x electrocatalyst with core shell structure in overall water splitting reactions, Chem. Eng. J. 485 (2024) 149903, https://doi.org/10.1016/j.cej.2024.149903.

[18] S. Banerjee, A. Kakekhani, R.B. Wexler, A.M. Rappe, Relationship between the Surface Reconstruction of Nickel Phosphides and Their Activity toward the Hydrogen Evolution Reaction, ACS Catal. 13 (2023) 4611–4621, https://doi.org/10.1021/acscatal.2c06427.

[19] A.B. Laursen, K.R. Patraju, M.J. Whitaker, M. Retuerto, T. Sarkar, N. Yao, K. V. Ramanujachary, M. Greenblatt, G.C. Dismukes, Nanocrystalline Ni_5P_4: a hydrogen evolution electrocatalyst of exceptional efficiency in both alkaline and acidic media, Energy Environ. Sci. 8 (2015) 1027–1034, https://doi.org/10.1039/C4EE02940B.

[20] Z. Huang, Z. Chen, Z. Chen, C. Lv, H. Meng, C. Zhang, $Ni_{12}P_5$ Nanoparticles as an Efficient Catalyst for Hydrogen Generation via Electrolysis and Photoelectrolysis, ACS Nano 8 (2014) 8121–8129, https://doi.org/10.1021/nn5022204.

[21] J.F. Callejas, C.G. Read, C.W. Roske, N.S. Lewis, R.E. Schaak, Synthesis, Characterization, and Properties of Metal Phosphide Catalysts for the Hydrogen-Evolution Reaction, Chem. Mater. 28 (2016) 6017–6044, https://doi.org/10.1021/acs.chemmater.6b02148.

[22] Z. Pu, J. Zhao, I.S. Amiinu, W. Li, M. Wang, D. He, S. Mu, A universal synthesis strategy for P-rich noble metal diphosphide-based electrocatalysts for the hydrogen evolution reaction, Energy Environ. Sci. 12 (2019) 952–957, https://doi.org/10.1039/C9EE00197B.

[23] Y. Pan, Y. Liu, J. Zhao, K. Yang, J. Liang, D. Liu, W. Hu, D. Liu, Y. Liu, C. Liu, Monodispersed nickel phosphide nanocrystals with different phases: synthesis, characterization and electrocatalytic properties for hydrogen evolution, J. Mater. Chem. A 3 (2015) 1656–1665, https://doi.org/10.1039/C4TA04867A.

[24] X. Zou, Y. Zhang, Noble metal-free hydrogen evolution catalysts for water splitting, Chem. Soc. Rev. 44 (2015) 5148–5180, https://doi.org/10.1039/C4CS00448E.

[25] Y. Shi, B. Zhang, Recent advances in transition metal phosphide nanomaterials: synthesis and applications in hydrogen evolution reaction, Chem. Soc. Rev. 45 (2016) 1529–1541, https://doi.org/10.1039/C5CS00434A.

[26] T. Liu, A. Li, C. Wang, W. Zhou, S. Liu, L. Guo, Interfacial Electron Transfer of Ni_2P–NiP_2 Polymorphs Inducing Enhanced Electrochemical Properties, Adv. Mater. 30 (2018) 1803590, https://doi.org/10.1002/adma.201803590.

[27] J. Zhang, T. Wang, D. Pohl, B. Rellinghaus, R. Dong, S. Liu, X. Zhuang, X. Feng, Interface Engineering of MoS_2/Ni_3S_2 Heterostructures for Highly Enhanced Electrochemical Overall-Water-Splitting Activity, Angew. Chem. Int. Ed. 55 (2016) 6702–6707, https://doi.org/10.1002/anie.201602237.

[28] C. Du, M. Shang, J. Mao, W. Song, Hierarchical MoP/Ni_2P heterostructures on nickel foam for efficient water splitting, J. Mater. Chem. A 5 (2017) 15940–15949, https://doi.org/10.1039/C7TA03669H.

[29] D. Chen, Z. Xu, W. Chen, G. Chen, J. Huang, C. Song, K. Zheng, Z. Zhang, X. Hu, H.-S. Choi, K. Ostrikov, Mulberry-Inspired Nickel-Niobium Phosphide on Plasma-Defect-Engineered Carbon Support for High-Performance Hydrogen Evolution, Small 16 (2020) 2004843, https://doi.org/10.1002/smll.202004843.

[30] D. Wang, Q. Duan, Z. Wu, Facile synthesis of MoP/MoO_2 heterostructures for efficient hydrogen generation, Mater. Lett. 241 (2019) 227–230, https://doi.org/10.1016/j.matlet.2019.01.095.

[31] Y. Luo, J. Jiang, W. Zhou, H. Yang, J. Luo, X. Qi, H. Zhang, D.Y.W. Yu, C.M. Li, T. Yu, Self-assembly of well-ordered whisker-like manganese oxide arrays on carbon fiber paper and its application as electrode material for supercapacitors, J. Mater. Chem. 22 (2012) 8634–8640, https://doi.org/10.1039/C2JM16419A.

[32] J.D. Roy-Mayhew, G. Boschloo, A. Hagfeldt, I.A. Aksay, Functionalized Graphene Sheets as a Versatile Replacement for Platinum in Dye-Sensitized Solar Cells, ACS Appl. Mater. Interfaces 4 (2012) 2794–2800, https://doi.org/10.1021/am300451b.

[33] Y. Wang, Y. Wang, J. Bai, W.-M. Lau, Trace Amount of NiP_2 Cooperative CoMoP Nanosheets Inducing Efficient Hydrogen Evolution, ACS Omega 6 (2021) 33057–33066, https://doi.org/10.1021/acsomega.1c05206.

[34] M.A. Ahsan, A.R. Puente Santiago, Y. Hong, N. Zhang, M. Cano, E. Rodriguez-Castellon, L. Echegoyen, S.T. Sreenivasan, J.C. Noveron, Tuning of Trifunctional NiCu Bimetallic Nanoparticles Confined in a Porous Carbon Network with Surface Composition and Local Structural Distortions for the Electrocatalytic Oxygen Reduction, Oxygen and Hydrogen Evolution Reactions, J. Am. Chem. Soc. 142 (2020) 14688–14701, https://doi.org/10.1021/jacs.0c06960.

[35] H. Jin, X. Liu, A. Vasileff, Y. Jiao, Y. Zhao, Y. Zheng, S.-Z. Qiao, Single-Crystal Nitrogen-Rich Two-Dimensional Mo_5N_6 Nanosheets for Efficient and Stable Seawater Splitting, ACS Nano 12 (2018) 12761–12769, https://doi.org/10.1021/acsnano.8b07841.

[36] H. Yin, S. Su, D. Yao, L. Wang, X. Liu, T.T. Isimjan, X. Yang, D. Cai, Ultrathin 2D–2D NiFe LDH/MOF heterojunction nanosheets: an efficient oxygen evolution reaction catalyst for water oxidation, Inorg. Chem. Front. 11 (2024) 2489–2497, https://doi.org/10.1039/D4QI00090K.

[37] L. Wang, H. Yu, Z. Huang, Z. Luo, T.T. Isimja, S. Xu, X. Yang, Interface engineering of porous nickel-iron phosphates with enriched oxygen vacancies as an efficient bifunctional electrocatalyst for high current water splitting, Electrochim. Acta 443 (2023) 141932, https://doi.org/10.1016/j.electacta.2023.141932.

[38] L. Cui, F. Chen, Y. Li, H. Hu, J. Li, J. Gao, X. Lin, Z. Chen, Construction of Ni_2P modified N-doped TiO_2 flower-like microspheres with rich 0D/2D heterojunctions for enhanced hydrogen evolution reaction, Mater. Today Chem. 37 (2024) 102025, https://doi.org/10.1016/j.mtchem.2024.102025.

[39] P. Yan, Y. Qin, Y. Yang, X. Shao, T.T. Isimjan, X. Yang, Controllable transformation of sheet-like CoMo-hydro(oxide) and phosphide arrays on nickel foam as efficient catalysts for alkali water splitting and Zn–H_2O cell, Int. J. Hydrogen Energy 47 (2022) 23530–23539, https://doi.org/10.1016/j.ijhydene.2022.05.136.

[40] B. Wang, H. Huang, M. Huang, P. Yan, T.T. Isimjan, X. Yang, Electron-transfer enhanced MoO_2-Ni heterostructures as a highly efficient pH-universal catalyst for hydrogen evolution, Sci. China Chem. 63 (2020) 841–849, https://doi.org/10.1007/s11426-019-9721-0.

[41] B. Liu, H. Li, B. Cao, J. Jiang, R. Gao, J. Zhang, Few Layered N, P Dual-Doped Carbon-Encapsulated Ultrafine MoP Nanocrystal/MoP Cluster Hybrids on Carbon Cloth: An Ultrahigh Active and Durable 3D Self-Supported Integrated Electrode for Hydrogen Evolution Reaction in a Wide pH Range, Adv. Funct. Mater. 28 (2018) 1801527, https://doi.org/10.1002/adfm.201801527.

[42] Y. Song, N. Li, D. Chen, Q. Xu, H. Li, J. He, J. Lu, 3D ordered MoP inverse opals deposited with CdS quantum dots for enhanced visible light photocatalytic activity, Appl. Catal. B Environ. Energy 238 (2018) 255–262, https://doi.org/10.1016/j.apcatb.2018.07.010.

[43] I. Jang, K. Im, H. Shin, K.-S. Lee, H. Kim, J. Kim, S.J. Yoo, Electron-deficient titanium single-atom electrocatalyst for stable and efficient hydrogen production, Nano Energy 78 (2020) 105151, https://doi.org/10.1016/j.nanoen.2020.105151.

[44] Y. Li, R. Li, D. Wang, H. Xu, F. Meng, D. Dong, J. Jiang, J. Zhang, M. An, P. Yang, A review: Target-oriented transition metal phosphide design and synthesis for water splitting, Int. J. Hydrogen Energy 46 (2021) 5131–5149, https://doi.org/10.1016/j.ijhydene.2020.11.030.

[45] L. Xiong, B. Wang, H. Cai, T. Yang, L. Wang, S. Yang, Neighboring effect induced by V and Cr doping in FeCoP nanoarrays for the hydrogen evolution reaction with Pt-like performance, J. Mater. Chem. A 8 (2020) 1184–1192, https://doi.org/10.1039/C9TA12562K.

[46] L. Wang, Y. Zhao, Z. Huang, X. Rao, M. Guo, T.T. Isimjan, X. Yang, Interfacial Regulation of Electron-enhanced Co_2P-CuP_2 Sheet-like Heterostructure as a Robust Bifunctional Electrocatalyst for Overall Water Splitting and $Zn-H_2O$ Cell, ChemCatChem 14 (2022) e202101933, https://doi.org/10.1002/cctc.202101933.

[47] M.-T. Chen, J.-J. Duan, J.-J. Feng, L.-P. Mei, Y. Jiao, L. Zhang, A.-J. Wang, Iron, rhodium-codoped Ni_2P nanosheets arrays supported on nickel foam as an efficient bifunctional electrocatalyst for overall water splitting, J. Colloid Interface Sci. 605 (2022) 888–896, https://doi.org/10.1016/j.jcis.2021.07.101.

[48] M. Guo, M. Xu, Y. Qu, C. Hu, P. Yan, T.T. Isimjan, X. Yang, Electronic/mass transport increased hollow porous Cu_3P/MoP nanospheres with strong electronic interaction for promoting oxygen reduction in Zn-air batteries, Appl. Catal. B Environ. Energy 297 (2021) 120415, https://doi.org/10.1016/j.apcatb.2021.120415.

[49] M. Gao, Z. Huang, L. Wang, H. Li, C. Ruan, R. Sadeq, T. Taylor Isimjan, X. Yang, Synergistic Co-N/V-N dual sites in N-doped $Co_3V_2O_8$ nanosheets: pioneering high-efficiency bifunctional electrolysis for high-current water splitting, J. Colloid Interface Sci. 658 (2024) 739–747, https://doi.org/10.1016/j.jcis.2023.12.064.

[50] M. Yu, Z. Wang, J. Liu, F. Sun, P. Yang, J. Qiu, A hierarchically porous and hydrophilic 3D nickel–iron/MXene electrode for accelerating oxygen and hydrogen evolution at high current densities, Nano Energy 63 (2019) 103880, https://doi.org/10.1016/j.nanoen.2019.103880.

[51] W. Xie, T. Yu, Z. Ou, J. Zhang, R. Li, S. Song, Y. Wang, Self-Supporting Clusters Constituted of Nitrogen-Doped $CoMoO_4$ Nanosheets for Efficiently Catalyzing the Hydrogen Evolution Reaction in Alkaline Media, ACS Sustain. Chem. Eng. 8 (2020) 9070–9078, https://doi.org/10.1021/acssuschemeng.0c02283.

[52] Y. Lu, Z. Li, Y. Xu, L. Tang, S. Xu, D. Li, J. Zhu, D. Jiang, Bimetallic Co-Mo nitride nanosheet arrays as high-performance bifunctional electrocatalysts for overall water splitting, Chem. Eng. J. 411 (2021) 128433, https://doi.org/10.1016/j.cej.2021.128433.

[53] B. Zhang, H. Xu, Q. Chen, H. Chen, G. He, ZIF-67 derived Mo_2N/Mo_2C heterostructure as high-efficiency electrocatalyst for hydrogen evolution reaction, J. Alloys Compd. 922 (2022) 166216, https://doi.org/10.1016/j.jallcom.2022.166216.

[54] T. Xiong, J. Li, J. Chandra Roy, M. Koroma, Z. Zhu, H. Yang, L. Zhang, T. Ouyang, M.S. Balogun, M. Al-Mamun, Hetero-interfacial nickel nitride/vanadium oxynitride porous nanosheets as trifunctional electrodes for HER, OER and sodium ion batteries, J. Energy Chem. 81 (2023) 71–81, https://doi.org/10.1016/j.jechem.2023.01.064.

[55] H. Yu, L. Wang, H. Li, Z. Luo, T.T. Isimjan, X. Yang, Improving the Electrocatalytic Activity of a Nickel-Organic Framework toward the Oxygen Evolution Reaction through Vanadium Doping, Chem. Eur. J. 28 (2022) e202201784, https://doi.org/10.1002/chem.202201784.

[56] M. Guo, Z. Huang, Y. Qu, L. Wang, H. Li, T.T. Isimjan, X. Yang, Synergistic effect and nanostructure engineering of three-dimensionally hollow mesoporous spherical Cu_3P/TiO_2 in aqueous/flexible Zn–air batteries, Appl. Catal. B Environ. Energy 320 (2023) 121991, https://doi.org/10.1016/j.apcatb.2022.121991.